Nonsteady discharge of granular media from a silo driven by a pressurized gas

Z. Zou,[1,2] P. Ruyer,[1] P.-Y. Lagrée,[3] and P. Aussillous[2,*]

[1]*Institut de Radioprotection et de Sûreté Nucléaire (IRSN), PSN-RES, SEMIA, LSMA, Cadarache, St Paul-Lez-Durance, 13115, France*

[2]*Aix-Marseille Université, CNRS, IUSTI, Marseille, 13013 France*

[3]*Sorbonne Université, CNRS UMR7190, Institut Jean le Rond ∂' Alembert, F-75005 Paris, France*

(Received 21 October 2021; accepted 6 May 2022; published 28 June 2022)

We studied experimentally and numerically the effect of an imposed gas pressure on the discharge flow of granular media from a cylindrical silo. This study is motivated by a nuclear safety related phenomenology of fuel fragments displaced from a fuel rod under several accidental conditions, the flow being potentially driven by pressurized fission gases within the rod. We imposed a moderate constant air pressure at the top of the granular column (≈3000 Pa) and we varied the size and type of the particles and the surrounding fluid where the discharge occurs, using air and water to test the role of the coolant fluid in the nuclear safety problem. The measured parameters are the particle mass flow rate, the volumetric flow rate of air, and the pressure along the silo. The particle and air flow rates are found to be nonsteady and to increase with time. To model these behaviors, we use a two-phase continuum model with a frictional rheology to describe particle-particle interactions, and we propose a simple quasisteady analytical model considering the air-pressure gradient at the orifice as an additional driving force to the gravity. We implemented numerically the two-phase continuum model in an axisymmetric configuration which reproduces the experimental results.

DOI: 10.1103/PhysRevFluids.7.064306

I. INTRODUCTION

The discharge flow of granular media from a silo is of practical interest in many industrial processes. Since the pioneer work of Hagen in 1852 [1] (translated in [2]), it is well known that the discharge flow of granular media from a silo is constant and depends mainly on the outlet dimensions, independently of the quantity of material in the silo. To predict this behavior, Hagen introduced the concept of a free fall arch at the outlet. By dimensional analysis, this arch scales with the outlet diameter D giving a velocity at the outlet of $v_0 \propto \sqrt{gD}$ and a flow rate $Q \propto \sqrt{gD^5}$. Even though this scaling reproduces well the experimental observations, it does not give a detailed understanding of the physical processes at plays in silo discharge. For example, Rubio-Largo *et al.* [3] have shown experimentally and using discrete simulations that instead of a free fall zone, an accelerating zone develops at the outlet scaling with the outlet diameter. Recently in the framework of a continuum modeling for the granular flows, it has been shown thanks to numerical simulation [4–8] that the shear-dependent frictional rheology $\mu(I)$ [9–11] reproduces qualitatively the granular discharge from a silo. In particular, the scaling of the flow rate is recovered. These studies suggest that close to the outlet, inertia dominates the flow and the frictional dissipation becomes negligible, in agreement with the scaling of the free fall arch concept. To take into account the small dependence

*pascale.aussillous@univ-amu.fr

of the flow rate on the particle diameter, d_p, Hagen [1] and Beverloo *et al.* [12] noted that the particles at the border of the outlet would partially lose their velocities and disrupt their neighbors, suggesting to use a reduce outlet diameter $(D - kd_p)$, where k is a fitting parameter. This leads to the simplest and widely used empirical expressions for a flat-bottomed silo, known as the Hagen-Beverloo relation. However, a recent work by Janda *et al.* [13], based on experimental measurements, suggests a different explanation. They have shown that the granular media tend to dilate at the outlet to maintain the discharge flow rate. The particle volume fraction at the outlet then depends on the ratio D/d_p, whereas the velocity still follows the previous scaling law.

Thus, for gravity driven flows of a given granular media, the outlet diameter appears as the only variable to control the flow rate in industrial situations. An existing method to overcome this situation and increase the discharge flow rate consists in pressurising the air in the silo, the subsequent relative motion of the interstitial fluid then blowing the material out of the silo [14]. The effect of interstitial pressure gradients on the discharge of granular materials has been studied in several geometrical configurations [14–20]. To model the grain-fluid coupling, most of the authors considered that the air pressure gradient acts as a driving force in addition to gravity. This gradient can be estimated thanks to classical models for flow through porous media. Recently, Zhou *et al.* [20] proposed to use a two-phase continuum model using the shear-dependent frictional rheology $\mu(I)$ for the particulate phase and the Darcy-Forchheimer resistance law for the drag force between the two phases [21]. They have shown that this model reproduces qualitatively the experimental results for a steady flow where a constant flow rate of air is injected at the top of a silo. This continuum model also validated an analytical model, where the driving fluid pressure gradient in addition to gravity corresponds to a mean gradient over a circular zone of size $D/2$ above the orifice where the particles accelerate.

However, few studies have been devoted to nonsteady discharge flow from silo driven by a pressurized gas. In particular, this configuration is relevant for the nuclear safety related issue. In the reactor pressure vessel of a pressurized water reactor of a nuclear power plant, the nuclear fuel is confined within fuel rods that are elongated cylinders (4 m long and 1 cm diam). This fuel initially consists of stack of 1-cm-long pellets, which are then fragmented into smaller pieces due to irradiation. The smallest fragments measure around tens of micron in the rim region. During a hypothetical reactivity initiated accident, the fuel and the rod are stressed due to a rapid and intense power peak. Some initially defected rods may then fail. Due to internal stresses and the potential presence of pressurized fission gases within the rod, fuel can be ejected toward surrounding water flow. Because the fuel fragments are at high temperature due to the power pulse, their interaction with the water could then induce a violent pressurization and vaporization, potentially hindering surrounding structures. The intensity of this interaction is strongly connected to the flow rate of fuel fragments out of the rod. Therefore, it is of interest to understand how this flow rate scales with the main parameters of the problem, such as failure opening, fragment sizes, and gas overpressure with respect to surrounding water. Due to the finite initial amount of gas within the rod, the gas flow will necessarily be unsteady. The experimental device somewhat simulates the situation using some idealizations of the process, namely the silo being the fuel rod, the granular media being the fuel, and the pressurized air being the fission gases. The impact of the surrounding fluid is also considered by immersing the silo in water.

The main objective of the present study is to investigate experimentally, analytically, and numerically how an imposed gas pressure at the top of a silo influences the discharge flow of granular media. One interesting feature of this configuration is that the particle and air flows are nonstationary, as can be seen in industrial situations. For experiments we mainly used model granular media composed of glass beads of uniform diameter, but we also used sand particles, having a more angular shape and a bidisperse mixture to test more realistic media. We studied the role of the surrounding fluid by discharging the silo mainly in air but also in water.

The article is organized as follows. In Sec. II, we present the experimental setup and the experimental observations. Then following previous authors [14–18,20], we develop in Sec. III a quasisteady analytical model to describe the observed behaviors. Finally in Sec. IV, thanks to a

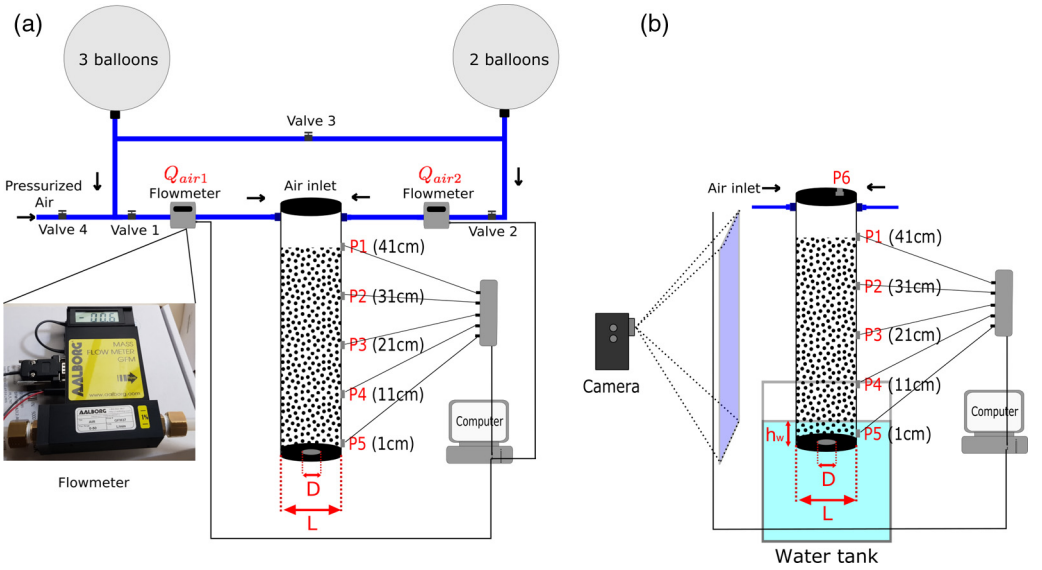

FIG. 1. (a) Experimental setup displaying the system of air injection with a constant pressure. (b) Schematic view of the experimental setup for studying the discharge of a silo immersed in water. The pressure taps are labeled P_i with the corresponding elevation with respect to the bottom given in brackets.

numerical simulation, we address the ability of the continuum model developed in [20] to reproduce the experimental results in an axisymmetric configuration.

II. EXPERIMENTAL OBSERVATIONS

A. Experimental setup

The experimental setup is illustrated in Fig. 1(a) for a discharge in air displaying the system of air injection, and in Fig. 1(b) for a discharge in water.

We use cylindrical silos of height $H = 0.5$ m and internal diameter $L = [20; 40; 60]$ mm. They are dismountable and composed of three parts: a top plug that can be removed in order to pour the particles into the silo, a main part in perspex with a thickness of 5 mm, and a changeable bottom plug with a circular outlet of diameter $D = [10; 20]$ mm located at its center. An o-ring seal is added to the bottom plug to ensure the tightness of the silo.

The silo is initially filled from the top with a total mass m_t of granular media, keeping the aperture closed. Three types of granular media are used: smooth spherical glass particles of mass density $\rho_p = 2500\ \mathrm{kg\,m^{-3}}$ (provided by Potter & Ballotini), smooth spherical ceramic particles of mass density $\rho_p = 6000\ \mathrm{kg\,m^{-3}}$ (provided by SiLibeads), and sand particles, having a more angular shape, of mass density $\rho_p = 2500\ \mathrm{kg\,m^{-3}}$ (provided by Sibelco). All the particles are sieved, and the mean size value is given in Table I, the dispersion in size being of $\pm 10\%$. We also studied the silo discharge for a bidisperse mixture, blending the same mass of ceramic particles of two sizes ($d_p = 180$ and 1165 μm). In this case, the column is filled by layers of 200 g, premixed in a container. Once the silo filled, the initial column height (h_p^0) is measured, varying between 32 and 40 cm. We deduce the initial bulk particle volume fraction $\phi_b = m_t/(\rho_p h_p^0 S_b)$, where S_b is the area of the silo cross section. The top of the silo is then closed.

A constant pressure of air (density $\rho_f = 1.2\ \mathrm{kg/m^3}$ and viscosity $\eta_f = 1.8 \times 10^{-5}$ Pa s) over the granular media during the discharge of the silo is obtained thanks to five latex balloons acting as a large reservoir of air. This reservoir is connected thanks to a system of valves to the top of the silo through two holes of diameter 4 mm (see Fig. 1). The balloons are separated into two groups of two

TABLE I. Performed experiments.

Granular media	Mean particle diameter d_p (μm)
Glass particles	[124; 190; 375; 538; 762; 1129; 1347] μm
Ceramic particles	[180; 550; 1165] μm
Sand	864 μm
Bidisperse mixture (ceramic particles)	50% mass of 180 and 1165 μm

and three balloons, respectively, connected through valve 3 that we keep opened during the entire process, ensuring the homogeneity of the pressure in all the balloons. To inflate the balloons, we open valve 4, close valves 1 and 2, and inject pressurized air into the balloons until they reach their maximum diameter of approximately 50 cm corresponding to an overpressure of ≈3000 Pa. Then, we close valve 4, we open valves 1 and 2, and the outlet is quickly opened manually. During the silo discharge, the pressurized air stored inside the balloons flows through the granular media. The total air flow rate is measured thanks to two flow meters (Aalgorg GFM mass flow meter with flow ranges of 0–5, 0–20, and 0–50 L/min with an accuracy of 1% and a response time of 1 s) located upstream to the two air inlets at the top of the silo, and it is determined by $Q_{\text{air}} = Q_{\text{air1}} + Q_{\text{air2}}$.

Simultaneously, the interstitial air pressure p^f along the silo is captured by five pressure sensors thanks to 3 mm holes drilled at different locations along a vertical axis as shown in Fig. 1. These holes are closed with a 40 μm mesh, and they are connected by a tube to one end of a differential piezoelectric pressure sensor, Honeywell DCAL405DN (range ±1245 Pa) or DCAL430DN (range ±7472 Pa), the other end being at the room pressure. The pressure signal is recorded during each run with an accuracy of ±0.25% and a frequency of 100 Hz. The air pressure above the granular column is given by the sensor P_1, as can be seen in Fig. 1. For all experiments we observe a quasiconstant level during the discharge with a relative variation below 10%.

When the discharge occurs in air, all the particles are collected by a metal vessel weighted by an electronic balance (Mettler Toledo 6002S) with a precision of 0.1 g at a frequency of 20 Hz. The instantaneous mass flow rate is obtained by processing the local slope of the mass versus time during $\delta t = 1$ s, $Q(t) = [m(t + \delta t) - m(t)]/\delta t$.

To study the discharge in water, the bottom of the silo is immersed in a rectangular water tank ($14 \times 35 \times 40$ cm^3) as shown in Fig. 1(b). This tank, made on glass to allow visualization, possesses a spillway 27.5 cm above the bottom to ensure a constant water level, h_w, above the silo bottom. A camera (GoPro) is placed in front of the silo to film the whole silo zone at an acquisition frequency of 240 frames per second and a resolution of 480×848 pixel^2 corresponding to a 60×30 cm^2 viewing zone of the silo. A rectangular light panel placed behind the silo provides a homogeneous white light source. A postprocessing of the pictures allows us to track the vertical position (h_p) of the top of the granular column within the silo and to deduce the temporal evolution of the particle mass ejected through the outlet, $m(t) = (h_p^0 - h_p)\rho_p\phi_b S_b$. The discharge flow rate of the granular media is then obtained as previously with $\delta t = 0.08$ s.

Each experiment is repeated at least twice with approximately the same experimental conditions: a small variation on the imposed initial air pressure level can be observed, as it depends slightly on the inflation size of the balloons; otherwise the results are fairly reproducible.

B. Typical results

We present in this section the results obtained for a silo of diameter $L = 40$ mm and an outlet size $D = 10$ mm: for those parameter values, we obtain a long discharge period as well as a good performance for maintaining a constant air pressure, which facilitates the analysis of the experimental results.

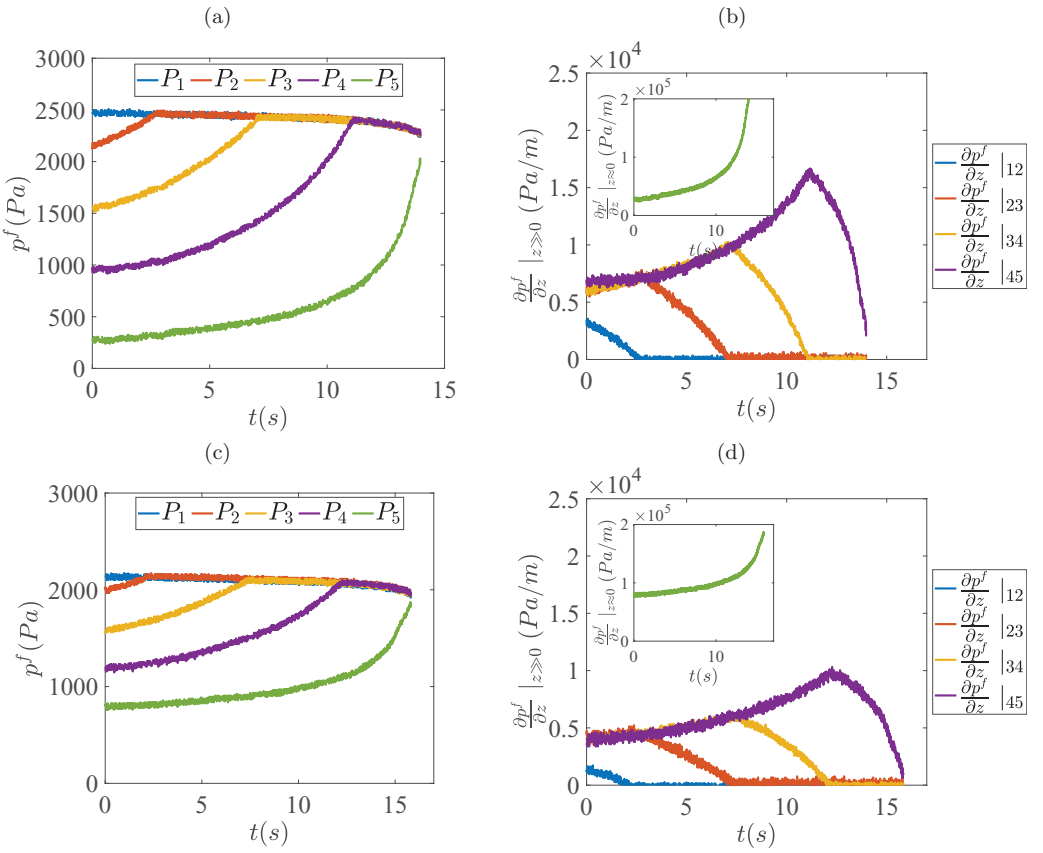

FIG. 2. Temporal evolution for (a),(c) the air pressure and (b),(d) the pressure gradient along a silo with $L = 40$ mm, $D = 10$ mm for ceramic particles ($d_p = 180\ \mu$m) discharging in (a),(b) air and (c),(d) water with $h_w \approx 50$ mm.

Thanks to the five pressure sensors, we measured the temporal evolution of the air pressure during the discharge. A typical evolution is represented in Fig. 2(a) for a discharge of ceramic particles ($d_p = 180\ \mu$m) in air. We observe that in this case, the total time of the discharge is around 14 s. The evolution of P_1 indicates a quasiconstant pressure level at the top of the silo during the discharge, with a tiny decrease leading to a relative variation below 10%. The pressures at the other elevations increase with time due to the decrease of the granular column height, and then they match with P_1 when the air column reaches the sensor position.

From the air pressure, we can deduce an estimation of the pressure gradients in the bulk of the silo, $(\partial p^f/\partial z)\,|_{ij} = (P_i - P_j)/(z_i - z_j)$, where i and j correspond to the index of the pressure sensors as shown in Fig. 1, and near the outlet, $(\partial p^f/\partial z)\,|_0 = P_5/z_5$. In Fig. 2(b) we observe that the pressure gradients in the bulk of the silo obtained with different pairs of sensors are superimposed while the pressure taps are immersed in the granular media. This suggests a vertical linear variation of the pressure in the bulk of the silo, corresponding to an incompressible flow. The air pressure gradient in the bulk of the silo increases more than linearly with time, and then the curves rapidly drop toward zero when the pressure taps are in the air part of the reservoir. Near the outlet [see the inset in Fig. 2(b)], the air pressure gradient is also found to increase similarly with time, but it is an order of magnitude larger than in the bulk of the silo. This is due to the restriction of the flow cross section at the outlet, which impacts the streamlines upstream on a typical length $h_1 \approx D$ [20].

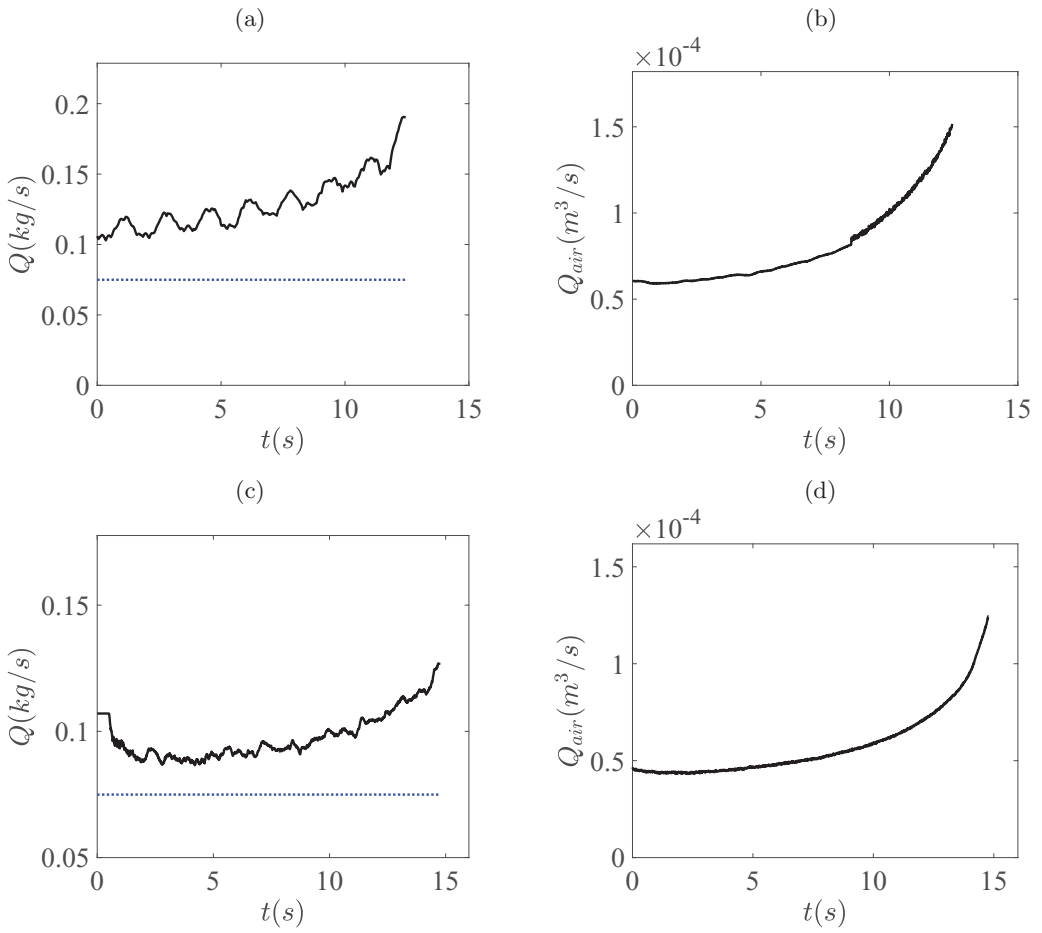

FIG. 3. Temporal evolution of (a),(c) the particle mass flow rate and (b),(d) the volumetric flow rate of air for $L = 40$ mm, $D = 10$ mm, and $d_p = 180$ μm (ceramic particles) for a discharge in air (a),(b) and in water (c),(d). The black lines correspond to the experimental measurements. The blue dotted lines represent the mean mass flow rate for a discharge in air without air injection, Q_0.

For a discharge in water, we observe mainly the same feature for the air pressure evolution [see Figs. 2(c) and 2(d)]. However, the pressure level inside the column and the pressure gradient near the outlet, P_5 and $(\partial p^f/\partial z)\,|_0 = P_5/z_5$, seem to be higher than on the dry case.

We now turn to the particle and air flow rates, as can be seen in Fig. 3 for a discharge in air or in water while maintaining a constant overpressure at the top of the silo. We observe that both flow rates increase more than linearly with time. In particular, the granular flow rate is significantly larger than the value Q_0 corresponding to the gravity-driven case. Indeed, during the silo discharge the height of the granular column decreases, which facilitates the passage of air and, simultaneously, increases the air pressure gradient through the granular media. As a result, the air flows at higher velocity, which results in an increasing drag on the particles, and thus an increasing granular flow rate with time. The oscillations observed on the particle flow rate for a discharge in air [Fig. 3(a)] are due to the electronic balance response and are not considered in the following (see Appendix A).

To interpret these results, in the next section we will adapt the analytical model developed by Zhou *et al.* [20] for a stationary gas-assisted discharge flow of granular media from silos, to the pressure-imposed configuration.

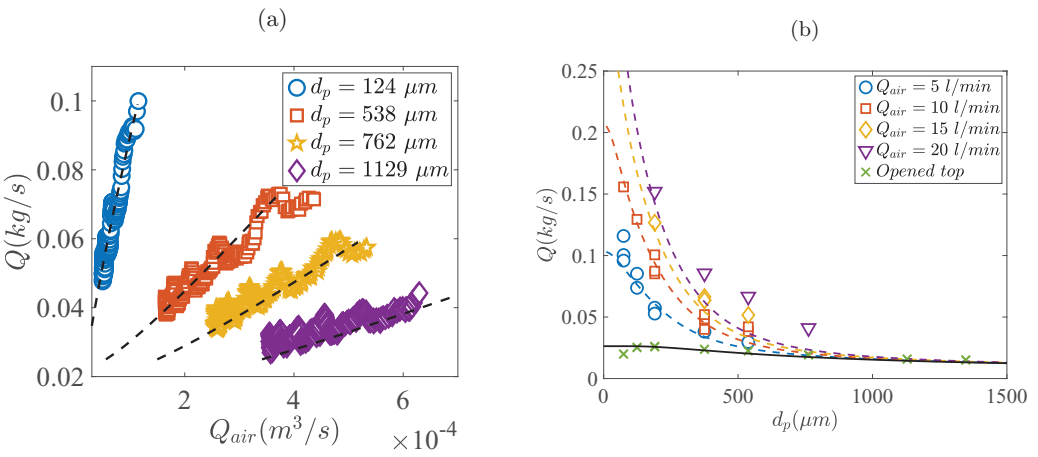

FIG. 4. (a) Particle mass flow rate as a function of the volumetric air flow rate for glass particles with $L = 40$ mm, $D = 10$ mm, and a discharge in air. (b) Particle mass flow rate as a function of the particle size for various instantaneous air flow rate for the same data. The straight line represents Eqs. (1) and (2) with $\alpha = 0.84$, $\beta = 0.07$. The dashed lines represent the analytical model developed by Zhou *et al.* [20] for a steady flow [Eq. (8)].

III. QUASISTEADY ANALYTICAL MODEL

A. Hypothesis of the model and experimental validation

In the previous section, we showed that a pressurized gas at the top of a silo leads to a nonstationary discharge flow. However, the time evolution of the particle and air flow rates stays moderate, as can be seen in Fig. 3. Based on this observation, we may assume the flow to be quasisteady. To test this hypothesis, in Fig. 4(a) we have plotted the particle flow rate versus the volume flow rate of air for various particle sizes for a discharge in air. For each particle size, we observe that the granular flow rate increases with the air flow rate similarly to steady flow [20], where the air flow rate at the top of the silo is constant. From the temporal evolution of the particle and air flow rate, we can also extract the particle flow rate for a given volume flow rate of air, as shown in Fig. 4(b) as a function of the particle diameter. The particle flow rate decreases when the particle size increases. Indeed, for a granular media composed of coarser particles, having a higher permeability, the air flow resistance is lower, corresponding to a lower driving force applied on the granular flow. We also plot on this graph the mass flow rate of the discharge driven by gravity without air injection ($\times$). The data are well adjusted using the expression given by Janda *et al.* [13]:

$$Q_0 = C\phi_0\rho_p\sqrt{g}D^{5/2}, \tag{1}$$

where g is the gravitational acceleration, ρ_p is the particle density, and C is a fitting parameter, and where the volume fraction at the center of the outlet accounts for the particle size dependence:

$$\phi_0 = \xi_\phi\phi_b\left[1 - \alpha e^{-\beta\frac{D}{d_p}}\right], \tag{2}$$

where ϕ_b is the bulk volume fraction, and ξ_ϕ, α, and β are fitting parameters. We obtained $\alpha = 0.82$ and $\beta = 0.07$, in good agreement with previous work in various configurations [8,13,20,22–24]. However, we observe a small discrepancy between the model and the experiment for the lower particle size where air countercurrent flow cannot be neglected. Interestingly, in Figs. 4(a) and 4(b) we observe that, except for the largest flow rate, the data with air injection are well adjusted by the analytical model developed by Zhou *et al.* [20] (see the dashed lines), which we outline as follows. Following [14–18], Zhou *et al.* [20] model the grain-fluid coupling by considering that the

air pressure gradient near the orifice acts as a driving force in addition to gravity:

$$Q = Q_0\left(1 + \frac{1}{\phi_0 \rho_p g}\frac{\partial p^f}{\partial z}|_o\right)^{1/2}, \tag{3}$$

where Q_0 represents the discharge flow rate without gas injection, and $\partial p^f/\partial z|_o$ is the air pressure gradient normal to the orifice at the outlet zone. To evaluate this term, Zhou *et al.* [20] first assume that the inertial, advective, buoyancy, and viscous stresses terms are negligible with respect to the drag force in the fluid momentum balance, which simply reduces to the balance between the fluid pressure gradient and the drag force. Then, they use the Darcy-Forchheimer resistance law to determine the drag force between air phase and granular media. Finally, they introduce the volume average velocity of the mixture, $U_i = \phi u_i^p + (1-\phi)u_i^f$, and they suppose that the streamlines are quasivertical both close to the orifice and in the bulk. The local relative velocity between the mixture and particles at the orifice, $v_{\rm rel}|_0 = [U_z|_0 - u_z^p|_0]$, can be deduced from a mass balance across the silo assuming incompressibility:

$$v_{\rm rel}|_0 = \frac{Q_{\rm air} - Q/(\phi_0 \rho_p)}{S_0} \tag{4}$$

with S_0 the orifice cross section, $Q_{\rm air}$ the air volume flow rate, and Q the particle mass flow rate. The pressure gradient at the outlet zone then reads

$$\frac{\partial p^f}{\partial z}|_0 \approx \frac{\eta_f}{\kappa_v(\phi_0, d)}\, v_{\rm rel}|_0 + \frac{\rho_f d}{\kappa_i(\phi_0)}\,[v_{\rm rel}|_0]^2, \tag{5}$$

where the coefficients of the Darcy-Forchheimer law are

$$\kappa_v = (1-\phi)^3 d^2/(150\phi^2) \text{ and } \kappa_i = (1-\phi)^3 d^2/(1.75\phi), \tag{6}$$

namely the Kozeny-Carman coefficient and the Ergun coefficient. The equations are normalized using $\rho_p g D$ as a pressure scale, the outlet size D as a lengthscale, and $\sqrt{D/g}$ as a timescale, except for the flow rate that is made dimensionless using the gravity-driven particle flow rate Q_0. The dimensionless parameters are denoted with a tilde; in particular, $\tilde{Q} = Q/Q_0$ is the dimensionless particle flow rate, and $\tilde{Q}_{\rm air} = \phi_0 \rho_p Q_{\rm air}/Q_0$ is the dimensionless air flow rate. Then, Eq. (3) can be written

$$\frac{\partial \tilde{p}^f}{\partial \tilde{z}}\,|_0 = \phi_0(\tilde{Q}^2 - 1). \tag{7}$$

By identification with Eq. (5), Zhou *et al.* [20] obtain a quadratic equation whose positive root gives the particle flow rate for a given air flow rate that reads as follows for a downward air flow:

$$\tilde{Q} = \frac{(-2\mathcal{N}_{i0}\tilde{Q}_{\rm air} - \mathcal{N}_{v0}) + \sqrt{\Delta}}{2(1-\mathcal{N}_{i0})} \quad \text{with} \quad \Delta = \mathcal{N}_{v0}^2 + 4(1 + \mathcal{N}_{v0}\tilde{Q}_{\rm air}) + 4\mathcal{N}_{i0}\left(\tilde{Q}_{\rm air}^2 - 1\right), \tag{8}$$

where we introduced $\mathcal{N}_{v0} = \eta_f Q_0/[\phi_0^2 \rho_p^2 \kappa_v(\phi_0, d) g S_0]$ and $\mathcal{N}_{i0} = \rho_f d_p Q_0^2/[\phi_0^3 \rho_p^3 \kappa_i(\phi_0, d) g S_0^2]$. The good agreement in Fig. 4 between the experimental data with air injection and Eq. (8) for most of the flow rates suggests that this analytical model can be adapted to the pressure-imposed configuration by considering a quasisteady flow, as is done in the following section.

In Ref. [20], air was injected at a constant flow rate, which imposes a constant pressure gradient near the orifice. In this study, during the discharge of the silo, the air pressure at the top of the silo is maintained at a quasiconstant level, which corresponds to a quasiconstant total pressure drop of air across the silo Δp^f. For a discharge in air, this pressure drop is simply given by the upper sensor, $\Delta p^f = P_1$, where we use the mean value over the discharge. For a discharge in water, the outlet pressure, $P^f_{\rm outlet}$, depends on the water depth above the silo outlet, h_w [see Fig. 1(b)]. To quantify this dependence, we performed experiments with an injection of a steady air flow rate from the silo top (see Appendix B). We found that the surrounding liquid adds a hydrostatic overpressure at the

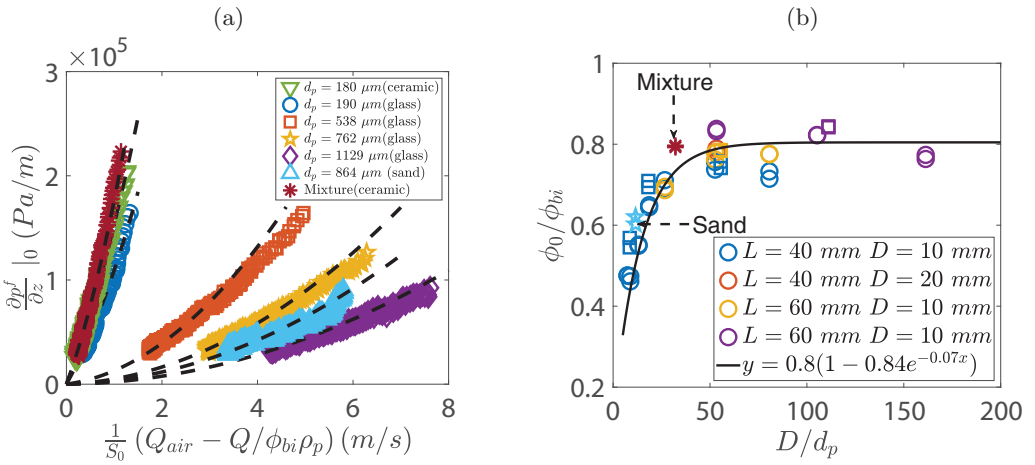

FIG. 5. (a) Experimental pressure gradient near the outlet as a function of $[Q_{\rm air} - Q/\rho_p\phi_{bi}]/S_0$ with $L = 40$ mm and $D = 10$ mm for various particle sizes d_p for monodisperse beads, and for the sand particles and the bidisperse mixture (see Table I). The dashed lines represent Eq. (5) with the fitting parameter ϕ_0. (b) The obtained fitting parameter ϕ_0 normalized by the initial bulk volume fraction ϕ_{bi} as a function of aspect ratio D/d_p for various silo diameters L and outlet sizes D for glass particles (circles), ceramics particle (squares), and for the sand particles and the bidisperse mixture. The black solid line represents Eq. (2) with $\xi_\phi = 0.80$, $\alpha = 0.84$, and $\beta = 0.07$.

outlet, $P^f_{\rm outlet} = P_{\rm atm} + \rho_w g(h_w + h_0)$, where $P_{\rm atm}$ represents the room air pressure and $h_0 \approx 1$ cm seems to correspond to the height of a bubble, observed in our experiments, located beneath the bottom of the silo during the discharge. The total pressure drop of air across the silo then reads $\Delta p^f = P_1 - \rho_w g(h_w + h_0)$, where we use the mean value over the discharge.

Based on the experimental observations [see Figs. 2(b) and 2(d)], we separate the granular column into two zones: the upper zone where the pressure gradient is uniform, and the bottom zone close to the orifice where it is larger. We then express the total pressure drop of the fluid as

$$\Delta p^f = h_1 \frac{\partial p^f}{\partial z}(t) \mid_0 + [h_p(t) - h_1]\frac{\partial p^f}{\partial z}(t) \mid_b, \tag{9}$$

where h_p represents the column height, $(\partial p^f/\partial z) \mid_0$ represents the pressure gradient near the outlet for $z < h_1$, and $(\partial p^f/\partial z) \mid_b$ represents the pressure gradient in the bulk far from the outlet for $z > h_1$, which we assume to be uniform along the granular column. The transition between the two zones is supposed to occur for $h_1 \simeq D$ as the jump of the pressure gradient appears at the scale of the outlet size.

Following [14–18,20], we model the grain-fluid coupling by considering that the air pressure gradient near the orifice acts as a driving force in addition to gravity [Eq. (3)], where the mass flow rate of the discharge driven by gravity without air injection, Q_0, is given by Eqs. (1) and (2) with $\alpha = 0.82$ and $\beta = 0.07$ as seen previously.

To evaluate both air pressure gradients, we follow Zhou *et al.* [20] and we suppose that we can neglect the inertial, advective, buoyancy, and viscous stress terms with respect to the drag force as $\rho_f \ll \rho_p$, $D \gg d$ and the Froude number defined on the particle length $\mathrm{Fr}_p = (u^f - u^p)^2/gd \approx Q^2_{\rm air}/(gdD^2) \gg \kappa_i d^{-2}$. Then, as the particulate Reynolds number of air, given by $\mathrm{Re}_p = \rho_f u^f d_p/\eta \sim \rho_f Q_{\rm air} d_p/(\eta S_0)$, varies in a range of 1–800, we also use the Darcy-Forchheimer resistance law to determine the drag force between air phase and granular media.

As shown by Zhou *et al.* [20], the pressure gradient at the outlet zone is then given by Eq. (5), where all the quantities should be considered as instantaneous. To validate this equation, in Fig. 5(a)

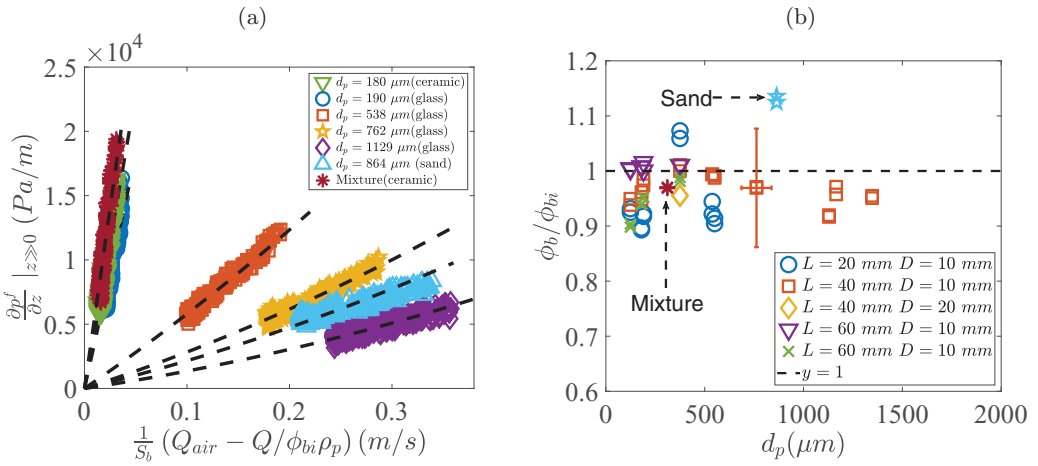

FIG. 6. (a) Experimental pressure gradient in the bulk as a function of $[Q_{\text{air}} - Q/\rho_p\phi_{bi}]/S_b$ with $L = 40$ mm and $D = 10$ mm for various particle sizes d_p for monodisperse beads, and for the sand particles and the bidisperse mixture (see Table I). The dashed lines represent Eq. (11) with the fitting parameter ϕ_b. (b) The obtained fitting parameter ϕ_b normalized by the initial bulk volume fraction ϕ_{bi} as a function of aspect ratio D/d_p for various silo diameters L and outlet sizes D for glass particles (circles), ceramics particle (squares), and for the sand particles and the bidisperse mixture. The dashed line represents $\phi_b = \phi_{bi}$.

we have plotted the experimental pressure gradient at the outlet versus $v_{\text{rel}}|_{(0)}$ [using for simplicity the initial bulk volume fraction in Eq. (4)] for various particle size and granular media with $L = 40$ mm and $D = 10$ mm. We observe that the data are fairly well fitted by Eq. (5) using ϕ_0 as an adjustable parameter obtained using the least-squares method [see the dashed lines in Fig. 5(a)]. To model the permeability of the bidisperse mixture, we use the Sauter diameter $\bar{d}_p = 1/[X_f/d_p^f + (1 - X_f)/d_p^c]$, where X_f is the mass fraction of fine particles, d_p^f is the diameter of fine particles, and d_p^c is the diameter of coarse particles. In Fig. 5(b) we have plotted the particle volume fraction at the outlet, ϕ_0, obtained as a fitting parameter and normalized by the initial bulk volume fraction, versus the ratio D/d_p for all the granular media and the silo configuration studied. All the data are superimposed and are well adjusted by Eq. (2) with the same coefficients ($\alpha = 0.84$, $\beta = 0.07$) as for the gravity-driven experiment and with a fitting coefficient $\xi_\phi = 0.80$. This suggests that the dilation that occurs at the outlet due to geometrical constraints is not influenced by the air flow.

Similarly, we evaluate the air pressure gradient in the bulk by first deducing from a mass balance the local relative velocity between the mixture and particles $v_{\text{rel}}(t)|_b = [U_z(t)|_b - u_z^p(t)|_b]$:

$$v_{\text{rel}}(t)|_b = \frac{Q_{\text{air}}(t) - Q(t)/(\phi_b\rho_p)}{S_b}, \tag{10}$$

with S_b the silo cross section, $Q_{\text{air}}(t)$ the instantaneous volume flow rate of air, and $Q(t)$ the instantaneous particle mass flow rate. Then the pressure gradient in the bulk reads

$$\frac{\partial p^f}{\partial z}(t)|_b \approx \frac{\eta_f}{\kappa_v(\phi_b, d)}\, v_{\text{rel}}(t)|_b + \frac{\rho_f d}{\kappa_i(\phi_b)}\,[v_{\text{rel}}(t)|_b]^2, \tag{11}$$

where the coefficients of the Darcy-Forchheimer law are given by Eq. (6). To validate Eq. (11), we have plotted in Fig. 6(a) the experimental pressure gradient in the bulk [using $\partial p^f/\partial z(t)|_{45}$] versus $v_{\text{rel}}|_b$ [using, for simplicity, the initial bulk volume fraction in Eq. (10)] for various particle sizes and granular media with $L = 40$ mm and $D = 10$ mm. We observe that the data are fairly well fitted by Eq. (11) using ϕ_b as an adjustable parameter obtained using the least-squares method [see the dashed lines in Fig. 6(a)]. In Fig. 6(b) we have plotted the obtained bulk particle volume fraction,

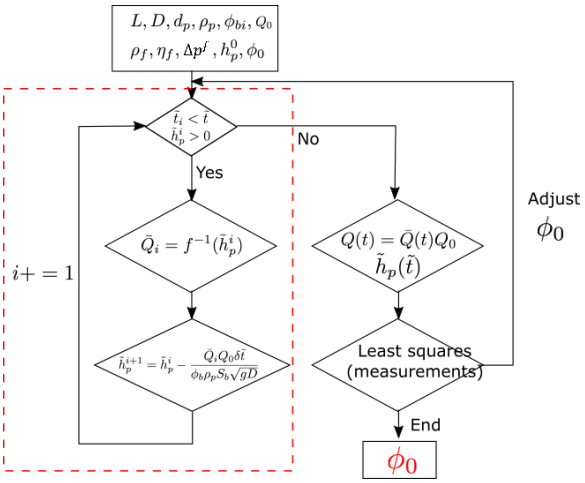

FIG. 7. Flow chart diagram of the numerical solver.

ϕ_b, normalized by the initial bulk volume fraction, versus the ratio D/d_p for all the granular media and the silo configuration studied. We obtain that the ratio ϕ_b/ϕ_{bi} falls in a range 0.9–1.1, which justifies that we will now assume for simplicity $\phi_b = \phi_{bi}$.

To obtain analytically the evolution of the granular column height $h_p(t)$, and subsequently the particle flow rate $Q(t)$ and the air volume flow rate $Q_{\text{air}}(t)$, we first normalize the equations as described previously for a steady flow. Then Eq. (8) can be rewritten to link the air flow rate to the particle flow rate:

$$\tilde{Q}_{\text{air}} = \tilde{Q} + \frac{\sqrt{\Delta} - \mathcal{N}_{v0}}{2\mathcal{N}_{i0}} \quad \text{with} \quad \Delta = 4\mathcal{N}_{i0}\tilde{Q}^2 - 4\mathcal{N}_{i0} + \mathcal{N}_{v0}^2. \tag{12}$$

Note that the discriminant Δ is strictly positive as $\tilde{Q} > 1$. Introducing in Eq. (9) the pressure gradient near the outlet given by Eq. (7) and the pressure gradient in the bulk given by Eq. (11), together with Eq. (12), we thus obtain an expression linking the particle flow rate with the granular column height:

$$\tilde{h}_p = \frac{\Delta\tilde{p}^f - \tilde{h}_1\phi_0(\tilde{Q}^2 - 1)}{\mathcal{N}_{vb}\phi_b\left(\frac{\phi_b}{\phi_0}\frac{\sqrt{\Delta}-\mathcal{N}_{v0}}{2\mathcal{N}_{i0}} - \tilde{Q}\right) + \mathcal{N}_{ib}\phi_b\left(\frac{\phi_b}{\phi_0}\frac{\sqrt{\Delta}-\mathcal{N}_{v0}}{2\mathcal{N}_{i0}} - \tilde{Q}\right)^2} + \tilde{h}_1. \tag{13}$$

Finally, the variation of the granular height $\tilde{h}_p$ with time is given by the particle velocity far from the outlet, with the assumed incompressibility reading as

$$\frac{d\tilde{h}_p}{d\tilde{t}} = \tilde{u}_z^p\,|_{z\gg 0} = \frac{-\tilde{Q}Q_0}{\phi_b\rho_p S_b\sqrt{gD}} \quad \text{with the initial condition} \quad \tilde{h}_p(t=0) = \tilde{h}_p^0. \tag{14}$$

B. Numerical solver

To solve this problem, and according to the experimental observation, we suppose that the particle volume fraction far from the outlet keeps its initial value, $\phi_b = \phi_{bi}$, and that $h_1 = D$ as the jump of the pressure gradient appears at the scale of the outlet size. Therefore, the only adjustable parameter in Eq. (13) is the volume fraction at the outlet ϕ_0. Equations (13) and (14) are solved numerically thanks to a dedicated *Matlab* script. Equation (14) is discretized using an Euler explicit method with a time step $\delta t = 0.05$ s, similar to the frequency of acquisition of the electronic balance.

A flow chart diagram of the numerical solver is displayed in Fig. 7. The entrance variables at the initial time step t_0 contain the experimental parameters (L, D, d_p, η_f, ρ_p), the experimental

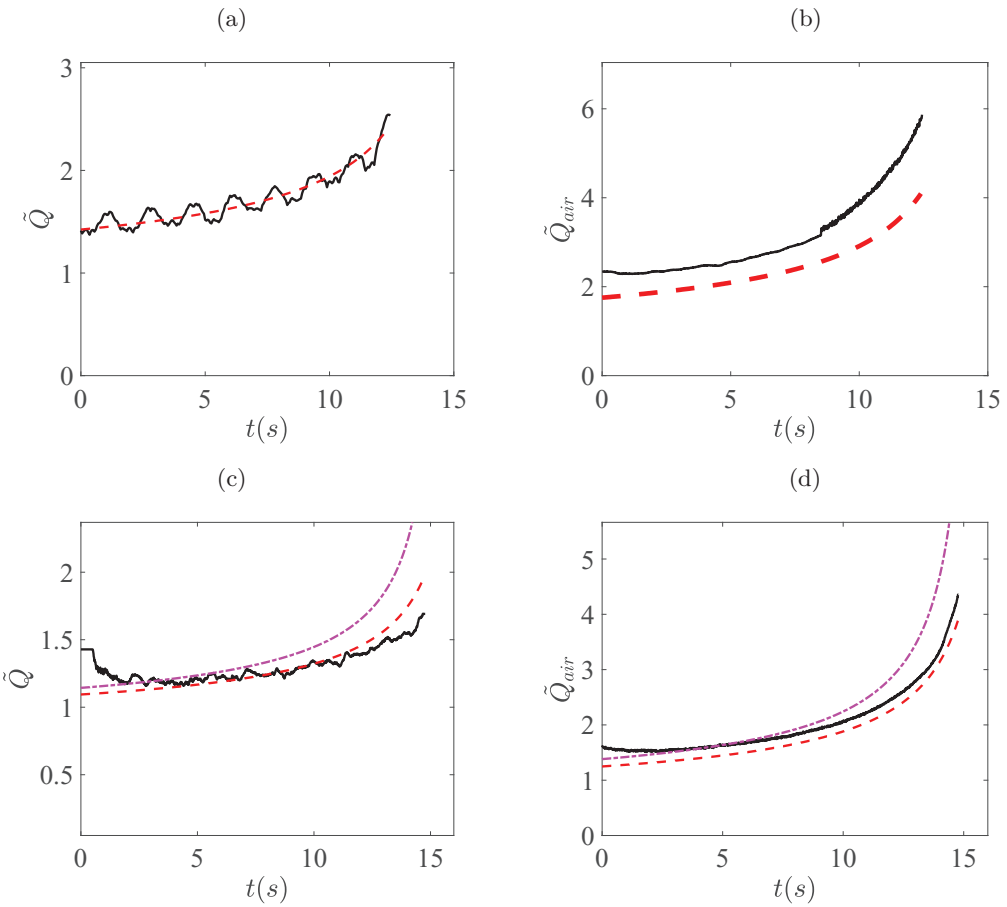

FIG. 8. Comparison of the experimental measurements with the results predicted by the quasisteady model for the temporal evolution of (a),(c) the dimensionless particle flow rate and (b),(d) the dimensionless volumetric flow rate of air for $L = 40$ mm, $D = 10$ mm, and $d_p = 180$ μm (ceramic particles) for a discharge in air (a),(b) and in water (c),(d). The red dashed lines represent the analytical model [Eqs. (13) and (14)] with (a),(b) $\phi_0 = 0.48$ and (c),(d) $\phi_0 = 0.44$. The purple dashed-dotted line represents the same model neglecting the overpressure due to water [Eq. (B1)].

conditions (h_p^0, ϕ_b), the total pressure drop, Δp^f, and the experimental discharge flow rate driven by gravity, Q_0. We impose a first value for $\phi_0 = 0.3$. For each discrete time step $\tilde{t}_i$ (see the part framed by the red dashed lines in Fig. 7), the nondimensional discharge flow rate of particles $\bar{Q}_i$ is calculated according to the inverse function of Eq. (13). Then, the next iteration granular column height $\tilde{h}_p^{i+1}$ can be determined by Eq. (14). This computing loop is run while $\tilde{h}_p$ stays positive. Therefore, this loop provides a prediction of the discharge flow rate $Q(t)$ as a function of time linked to a prescribed value of ϕ_0. This prediction is compared to the temporal evolution of the experimental discharge flow rate, and the fitting value of ϕ_0 is obtained using the least-squares method.

C. Comparison with experiments

In Fig. 8(a) we observe a good agreement between the model and the experimental dimensionless mass flow rate, upon which the least-squares method is based, for a granular media composed of spherical monodisperse particles. In Fig. 8(b) we also observe a fairly good agreement between the

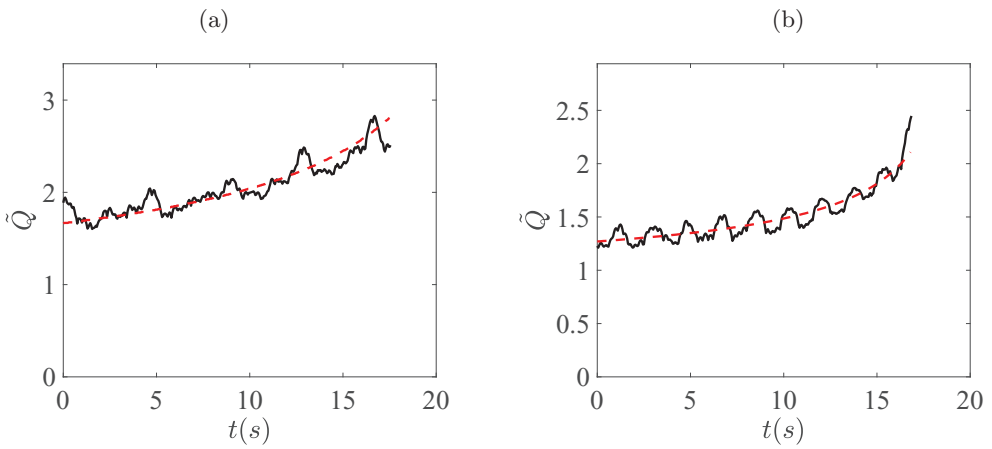

FIG. 9. Comparison of the experimental temporal evolution of the dimensionless particle flow rate with the results predicted by the quasisteady model (red dashed line) for $L = 40$ mm, $D = 10$ mm for (a) the sand particles ($d_p = 864$ μm) and (b) the bidisperse mixture (ceramic particles with 50% mass of $d_p = 1165$ and 180 μm).

experimental volume flow rate of air entering into the silo during the discharge and the model deduced from Eqs. (13) and (14). The model predicts also fairly well the dynamic of a silo discharge in water, as can be seen in Figs. 8(c) and 8(d), taking into account in Δp^f the overpressure at the outlet [Eq. (B1)] due to the water column (see the dashed red line). Neglecting the overpressure leads to an overestimation of the flow rates with the same ϕ_0 (see the purple dashed-dotted line). We also observe that the model gives a good prediction of the experimental results for the sand particles [see Fig. 9(a)] and the bidisperse mixture [see Fig. 9(b)].

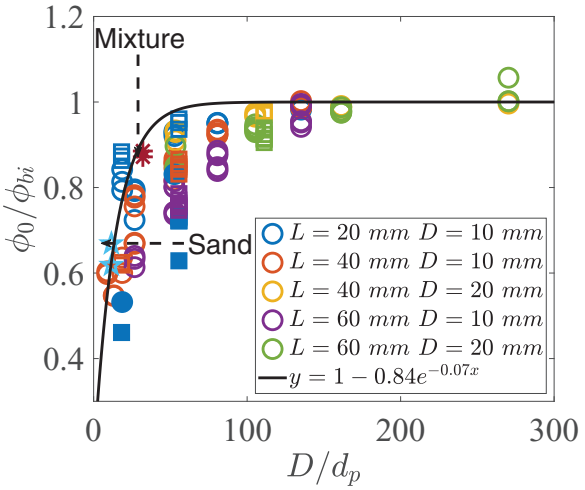

FIG. 10. Obtained fitting parameter ϕ_0 normalized by the initial bulk volume fraction ϕ_{bi} as a function of the aspect ratio D/d_p for various silo diameters L and outlet sizes D for glass particles (circles), ceramics particle (squares), sand particles, and for the bidisperse mixture. The empty symbols correspond to a silo discharge in air, and the full symbols correspond to a silo discharge in water. The black solid line represents Eq. (2) with $\xi_\phi = 1$, $\alpha = 0.84$, and $\beta = 0.07$.

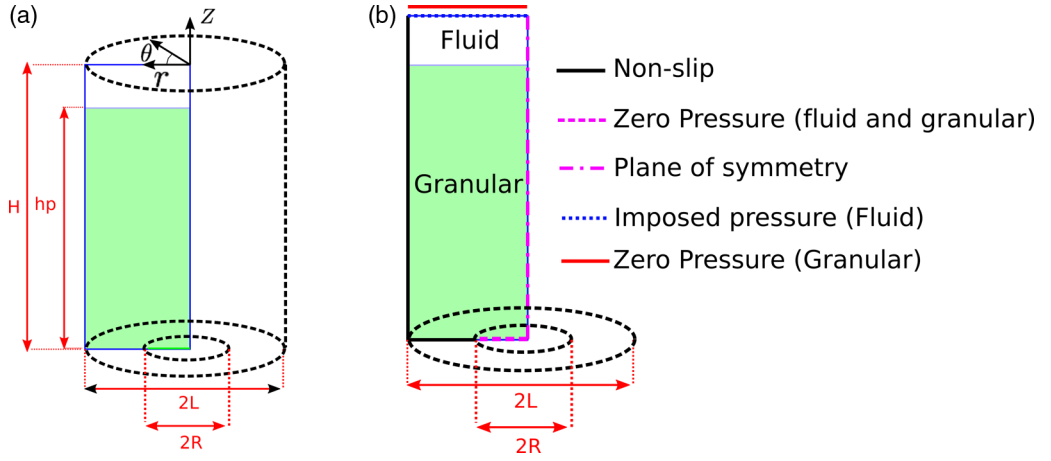

FIG. 11. (a) Configuration and (b) boundary conditions of the continuum simulation for the discharge of a silo with a pressurized gas at its top in a cylindrical geometry.

Finally, in Fig. 10 we have plotted the obtained value of ϕ_0, normalized by ϕ_{bi}, as a function of the ratio D/d_p, for various silo diameters L and outlet sizes D, for all the granular media studied, and for a discharge in air (empty symbols) or in water (full symbols). We observe that the data are a little bit scattered but superimpose reasonably and are well represented by Eq. (2) (see the full line in Fig. 10) with the same coefficients α and β as for the gravity-driven experiment and with the fitting parameter $\xi_\phi = 1$. This suggests that the steric effect due to the finite size of the particle compared to the outlet size is scarcely influenced by the air flow. Moreover, the good collapse of the experimental results for the sand particles and the bidisperse mixture tends also to suggest that the permeability is the main parameter in this experiment. We also observe that the surrounding fluid does not play a significant role in the discharge. Using a gravity-driven experiment to calibrate α and β, we can thus fully predict the temporal evolution of the discharge flow of a granular media from a silo with an imposed air pressure at its top. Let us note that the value of ξ_ϕ differs slightly from the one determined with the gradient of pressure near the outlet [see Fig. 5(b)], which may suggest that this parameter also accounts for the zone of evaluation of the pressure gradient as seen in Ref. [20]. This will be discussed in the following section, where we test the ability of a two-phase continuum model with $\mu(I)$ frictional rheology for the granular phase to predict the discharge flow from a silo with an imposed pressure at its top in a cylindrical geometry.

IV. CONTINUUM SIMULATION

A. Two-phase continuum modeling

Following Zhou *et al.* [20], we consider a two-phase continuum model to capture the coupling between the air and the granular material during the discharge of the silo. This two-fluid flow out of a cylindrical silo with a pressurized air flow can be considered as an axisymmetric flow with no azimuthal velocity. Therefore, we use the cylindrical coordinate system, where r stands for the radial direction and z for the vertical direction, the coordinates being drawn in Fig. 11(a). We write the mass conservation equations for both phases, fluid and particles:

$$\frac{\partial\left(ru_r^f\right)}{\partial r} + \frac{\partial\left(ru_z^f\right)}{\partial z} = 0, \tag{15}$$

$$\frac{\partial\left(ru_r^p\right)}{\partial r} + \frac{\partial\left(ru_z^p\right)}{\partial z} = 0. \tag{16}$$

The momentum conservation equations for both phases read

$$-R_f\frac{\partial u_r^f}{\partial t}-\frac{\partial p^f}{\partial r}-B_v\left(u_r^f-u_r^p\right)-B_i\left(u_r^f-u_r^p\right)\left|u_r^f-u_r^p\right|\,|=0, \tag{17}$$

$$-R_f\frac{\partial u_z^f}{\partial t}-\frac{\partial p^f}{\partial z}-B_v\left(u_z^f-u_z^p\right)-B_i\left(u_z^f-u_z^p\right)\left|u_z^f-u_z^p\right|=0, \tag{18}$$

$$-\rho\left[\frac{\partial u_r^p}{\partial t}+u_r^p\frac{\partial u_r^p}{\partial r}+u_z^p\frac{\partial u_r^p}{\partial z}\right]+\frac{1}{r}\frac{\partial\left(r\sigma_{rr}^p\right)}{\partial r}+\frac{\partial\sigma_{zr}^p}{\partial z}-\frac{\partial p^f}{\partial r}=0, \tag{19}$$

$$-\rho\left[\frac{\partial u_z^p}{\partial t}+u_r^p\frac{\partial u_z^p}{\partial r}+u_z^p\frac{\partial u_z^p}{\partial z}\right]+\frac{\partial\sigma_{zz}^p}{\partial z}+\frac{1}{r}\frac{\partial\left(r\sigma_{rz}^p\right)}{\partial r}-\frac{\partial p^f}{\partial z}-\rho g=0. \tag{20}$$

For the fluid phase [(17) and (18)] the drag force between the granular phase and the gas phase is modeled by the Darcy-Forchheimer resistance law, where $B_v=\eta(1-\phi)/\kappa_v$ and $B_i=\rho_f d(1-\phi)^2/\kappa_i$. Additionally, $R_f=\rho_f[1+C_{\rm vm}\phi/(1-\phi)]$ represents a virtual mass approach taking unsteady effects into account in the fluid phase [25–28], where $C_{\rm vm}=2$ is an empirical coefficient (in the range of $0.5\leqslant C_{\rm vm}\leqslant 2.0$ [29]) and $\phi=0.6$ is the volume fraction of granular media. In the granular phase [(19) and (20)], we use the shear-dependent frictional rheology [9–11]:

$$\sigma_{ij}^p=\eta_p\gamma_{ij}\quad\text{with }\eta_p(|\dot\gamma|,p^p)=\frac{\mu(I)p^p}{|\dot\gamma|}, \tag{21}$$

where $\dot\gamma_{ij}$ is the strain-rate tensor (for example, $\dot\gamma_{rz}=\partial u_r^p/\partial z+\partial u_z^p/\partial r$) with $|\dot\gamma|=\sqrt{(\dot\gamma_{ij}\dot\gamma_{ij}/2)}$ its second invariant. The friction function of the $\mu(I)$-rheology is defined as

$$\mu(I)=\mu_s+\Delta\mu/(I_0/I+1)\text{ with }I=|\dot\gamma|d/\sqrt{p^p/\rho_p},$$

where I_0, μ_s, and $\Delta\mu$ are constants that depend on the granular media. We do not take into account the shear-rate dependence of the volume fraction [11].

Note that the system of equations is made dimensionless for resolution using the silo diameter L as a lengthscale, ρgL as a pressure scale, and $\sqrt{L/g}$ as a timescale. Note as well that we use a regularization technique to avoid the divergence of the viscosity when the shear becomes too small by replacing η_p by $\min(\eta_p,\eta_{\rm max})$ with $\eta_{\rm max}=100\rho\sqrt{gL^3}$ a constant that is large enough [4,5,8,20,30].

B. Some details on numerical implementation

The free software Basilisk [31] resolves partial differential equations on adaptive Cartesian meshes. Libraries are developed to solve Navier-Stokes equations with a finite-volume projection method, and a volume-of-fluid method is used to track the two phases. To solve the coupled Eqs. (17)–(20), we consider the gas phase and the granular phase separately. We rewrite the momentum equation of the gas phase as

$$R_f\frac{\vec{u}^{\,f}_{n+1}-\vec{u}^{\,f}_{n}}{\Delta t}=-\vec{\nabla}p^f-B_l(\vec{u}^{\,f}_{n+1}-\vec{u}^{\,p})-B_i\,|\,\vec{u}^{\,f}_{n}-\vec{u}^{\,p}\,|\,(\vec{u}^{\,f}_{n+1}-\vec{u}^{\,p}), \tag{22}$$

and according to incompressibility (15) and (16), Eq. (22) can be written in the following form (reminiscent of the projection method itself):

$$\vec{\nabla}\cdot\left(\frac{r\Delta t\,\vec{\nabla}p^f}{R_f+\Delta t(B_l+B_i|\vec{u}^{\,f}_{n}-\vec{u}^{\,p}|)}\right)=\vec{\nabla}\cdot\left(r\frac{R_f\vec{u}^{\,f}_{n}+\Delta t(B_l\vec{u}^{\,p}+B_i\vec{u}^{\,p}|\vec{u}^{\,f}_{n}-\vec{u}^{\,p}|)}{R_f+\Delta t(B_l+B_i|\vec{u}^{\,f}_{n}-\vec{u}^{\,p}|)}\right). \tag{23}$$

Equation (23) is in the form of a Poisson-Helmholtz equation that we solve in Basilisk, using a specific solver [32]. Thus we obtain the pressure field of the fluid phase as well as the corresponding

pressure gradients, which corresponds to the drag forces that we impose on the granular media, in Eqs. (19) and (20). We solve them at each time step in a 2D axisymmetric configuration.

This configuration for studying the discharge of a silo with an imposed gas pressure at the top is displayed in Fig. 11(a). In the cylindrical coordinate, the calculation domain consists of a two-dimensional (2D) plane of width L and height $H = 4L$. The granular media is considered as a continuum media and has an initial height $h_p = 3.8L$. The width of the silo L is divided into 64 computation cells (leading to enough precision). An outlet of radius $R = D/2$ is placed at the right bottom of the calculation domain.

On the side walls [see the black lines in Fig. 11(b)], a Neumann boundary condition is applied both for the granular pressure and the fluid pressure together with a no-penetration condition as well as a nonslip condition. At the outlet, a Dirichlet boundary condition is applied [see the purple dashed line in Fig. 11(b)] for the pressure of the two phases ($p^p = 0$ and $p^f = 0$) together with a Neumann boundary condition for the normal and tangential components of the velocity for both phases. For the plane of symmetry [see the purple dashed-dotted line in Fig. 11(b)], a no-penetration condition is applied for the normal velocity component for both phases, and a free-slip boundary condition is applied for the tangential velocity component, along the vertical direction. Finally, for the top border of the calculation domain, a Dirichlet boundary condition is chosen for the pressure of the two phases, but with different values. For the fluid phase, $p^f = p_{\text{air}}$, where p_{air} represents the value of the fluid pressure imposed, and for the granular phase, $p^p = 0$. Additionally, the normal and tangential components of the velocity for both phases possess a Neumann boundary condition.

During the simulation, the velocity fields of both phases are calculated for every $\Delta t = 0.1/\sqrt{L/g}$. Therefore, the instantaneous mass flow rate of the granular phase and the volumetric flow rate of the fluid phase can be determined from the velocity fields by integrating the vertical velocity component across the outlet, $Q_i = \rho \int_0^R 2\pi r u_z^p \,|_{z=0}\, dr$ and $Q_{\text{air}} = \int_0^R 2\pi r u_z^f \,|_{z=0}\, dr$. The other fields, like the pressures, are saved during the simulation for every $\Delta t = 1/\sqrt{L/g}$.

C. Numerical results

We carried out a series of continuum simulations, varying the value of the imposed constant gas pressure p_{air} at the top of the silo and of the outlet radius R. The dimensionless coefficients in the drag force between the two phases are taken as $B_v = 25$ for the viscous term and $B_i = 6.3$ for the inertial term corresponding to the experimental conditions for a particle size of about 500 μm. We take for the rheological constants $\mu_s = 0.4$, $\Delta\mu = 0.28$, $I_0 = 0.4$. Additionally, the coefficient representing a virtual mass approach is set to a value of $R_f = 0.002\rho$.

In Fig. 12(a), the streamlines for both phases are displayed with red lines for the granular phase and green dotted lines for the fluid phase. We observe that both streamlines are vertical far from the outlet. Upon approaching the outlet due to the restricted cross section, the streamlines converge towards the outlet and the velocity increases. The flow at the outlet can be reasonably taken as vertical, as supposed in the analytical model. In the following part, we will discuss a typical example of numerical simulation, with an outlet radius $R = 0.25L$ and an imposed air pressure $p_{\text{air}} = 5\rho gL$.

The temporal evolution of the pressure profiles of the fluid phase $p^f/\rho gL$ for different positions along the silo is shown in Fig. 12(c), denoted by full lines at the side wall and dashed lines at the center [see Fig. 12(b) for the position of evaluation of the fluid pressure]. We observe a similar trend to that observed in the experiment [see Fig. 2(a)]: the pressure at a given position increases during the discharge period due to the decrease of the granular column height, and it finally reaches the imposed pressure level p_{air} when the tap is above the granular media. Moreover, we observe that the measurements at the side wall of the silo [see the full lines in Fig. 12(c)] give the same values as at the central line of the silo (dashed lines) as long as $z > 2R$, which validates using the experimental pressure measurements at the side wall of the silo to estimate the bulk values.

To compare the numerical results with the quasisteady analytical model for the discharge, we have first evaluated the pressure gradient of the fluid phase at the outlet. Note that in the simulation, the granular media is incompressible and $\phi_0 = \phi_{bi}$. Zhou *et al.* [20] have shown for

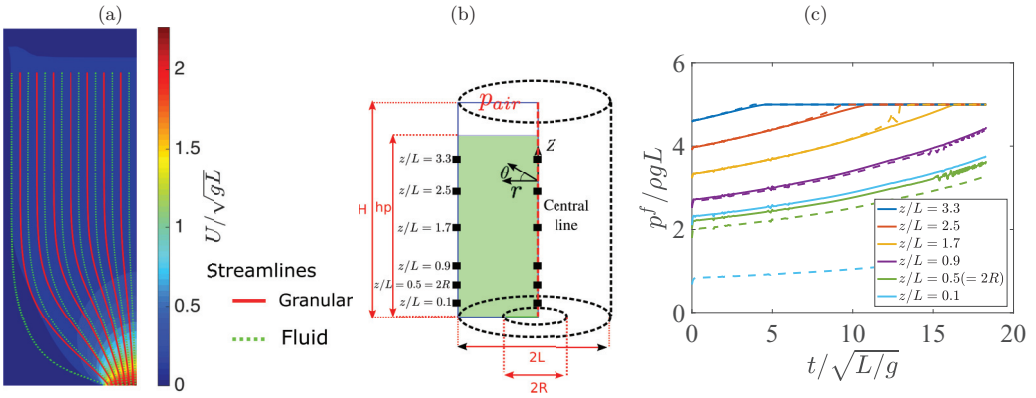

FIG. 12. (a) Magnitude of the velocity field for the granular phase and streamlines for the granular flow (red full lines) and for the gas flow (green dotted lines). (b) Sketch of the position of evaluation of the fluid pressure. (c) Temporal evolution of the fluid pressure for various vertical positions in the silo taken at the side wall (full lines) and at the central line (dashed lines) for $R = 0.25L$ and $p_{\rm air} = 5\rho gL$.

a simpler configuration (2D viscous flow) that the mean air pressure gradients near the orifice need to be evaluated over the zone of acceleration of the particles. Figure 13(a) shows the pressure gradient averaged on the outlet section, $(\partial p^f/\partial z)\,|_{(r<R)(z=0)} = (2/R^2)\int_0^R (\partial p^f/\partial z)\,|_{z=0}\, rdr$, and on an ellipsoidal zone above the outlet, $(\partial p^f/\partial z)\,|_{(\frac{r^2}{R^2}+\frac{z^2}{h_1^2}\leqslant 1)} = [3/(R^2 h_1)]\int_0^{h_1}(\int_0^R (\partial p^f/\partial z)\,|_{r,z}\, rdr)dz$, where $h_1 = D$. In each case, we observe that the averaged pressure gradient is proportional to $B_l(Q_{\rm air} - Q/\rho)/S_0 + B_i(Q_{\rm air} - Q/\rho)^2/{S_0}^2$, as supposed in the analytical model [Eqs. (4) and (5)] with, respectively, a multiplicative coefficient $\mathcal{A} = 1$ and 0.4. The coefficient $\mathcal{A}$ then accounts for the zone of evaluation of the pressure gradient similarly to the fitting parameter ϕ_0 in the experiments. Then, to compare with the numerical results, we use the analytical model given by Eqs. (13) and (14), replacing $\mathcal{N}_{v0}$ by $\mathcal{A}\mathcal{N}_{v0}$ and $\mathcal{N}_{i0}$ by $\mathcal{A}\mathcal{N}_{i0}$. In Fig. 13(b), we have plotted the temporal

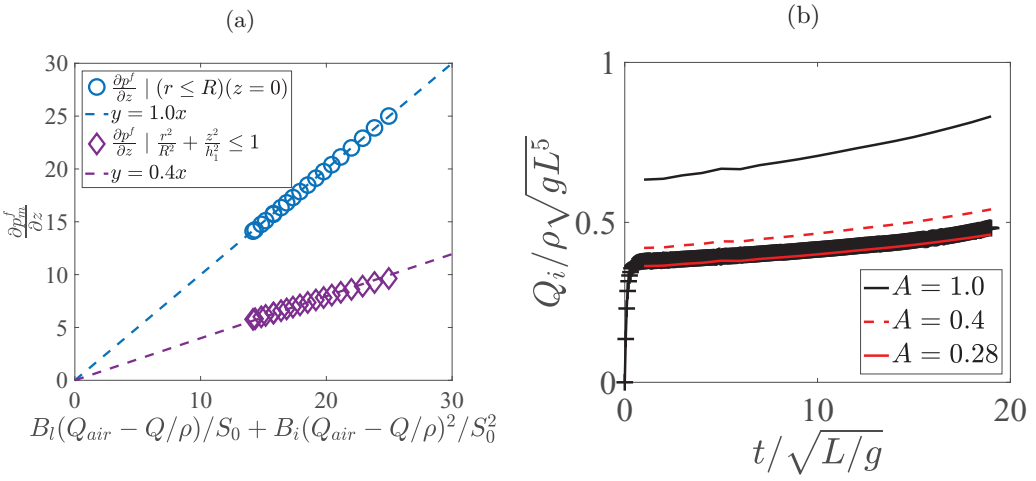

FIG. 13. (a) Average pressure gradients of the fluid phase on the outlet section (○) and on an ellipsoidal zone above the outlet (◊) as a function of $B_l(Q_{\rm air} - Q/\rho)/S_0 + B_i(Q_{\rm air} - Q/\rho)^2/{S_0}^2$. (b) Temporal evolution of the nondimensional discharge flow rate of the granular media $Q/\rho\sqrt{gL^5}$ for $R = 0.25L$ and $p_{\rm air} = 5\rho gL$ and comparison with the prediction of the model with different coefficient values $\mathcal{A}$.

evolution of the discharge flow rate of the granular media, and we compare it with the analytical model for $A = 1$ (black full line) and $A = 0.4$ (red line), corresponding to the volume average of the pressure gradient at the outlet. We observe a better agreement taking into account this parameter, the best fit being for $A = 0.28$, for which we observe a very good agreement between the numerical results and the quasisteady analytical model.

All of these results show the good ability of the two-phase modeling, with a frictional rheology for the granular phase and a Darcy-Forchheimer drag force, to reproduce the experimental results for the discharge of the silo with an imposed pressure at its top. This model and its numerical implementation could thus be used to predict the behavior for more complex geometrical situations.

V. CONCLUSION

We have investigated experimentally the discharge of a granular media from a silo coupled with an air flow due to a moderate imposed air pressure at the top of the silo. In this case, we observe that the particle flow rate increases with time together with the air flow rate, as the height of the granular column decreases. We have then related these flow rates variations to the time evolution of the pressure gradient along the granular column that is uniform in the upper part and larger near the outlet due to flow cross-section reduction. We have shown that the air flow does not modify the dilation of particles near the outlet with respect to the size ratio between particles and orifice. We have also investigated the effect of a surrounding liquid, and we have shown that the liquid just adds an overpressure at the outlet due to the hydrostatic pressure. Additionally, we have used several types of granular media (monodisperse spheres, bidisperse mixture, sand) of several sizes, and the results show that the permeability is the main parameter in this experiment. More experiments on bidisperse mixtures should be performed to confirm this preliminary result.

In the hypothesis of a quasisteady incompressible flow, we have proposed an analytical model, where the fluid pressure gradient near the orifice acts as an additional driving force with respect to gravity in accordance with previous authors [14–16,20], and the drag force between the two phases is given by the Darcy-Forchheimer resistance law, which accounts quite well for the experimental data. The effects of the silo dimension or of the particle sizes are fully recovered by the model, which allows us to predict the full discharge of the silo.

Finally, we have fully solved (in a 2D axisymmetric configuration) a continuum two-phase numerical model with a granular frictional rheology and a Darcy-Forchheimer resistance law between the phases. We have shown the ability of this model to reproduce the experimental observations and to validate the hypothesis of the analytical model.

In this work, we have studied a nonstationary flow. However, due to the moderate value of the imposed air pressure at the top of the silo, we have shown that the hypothesis of a quasisteady incompressible flow is valid. In future work, it would be interesting to test a configuration in which we impose a higher pressure and a violent rupture of the orifice, as can be seen in industrial situations, and where, therefore, the compressibility of air cannot be neglected.

ACKNOWLEDGMENTS

We would like to thank S. Noel and F. Ratouchniak for technical assistance. This work is funded by Institut de Radioprotection et de Sûreté Nucléaire (IRSN) and Électricité de France (EDF) in the frame of their collaborative research programs.

APPENDIX A: OSCILLATIONS OF THE DISCHARGE FLOW RATE

In the temporal evolution of the particle flow rate, as shown in Fig. 3(a), we observe that the discharge flow rate of the granular media seems to oscillate with a quite regular frequency. This puzzling feature was also observed in previous studies using the same apparatus [8,20,22] or in the literature [33]. To investigate the origin of these oscillations, we performed a discharge of the silo

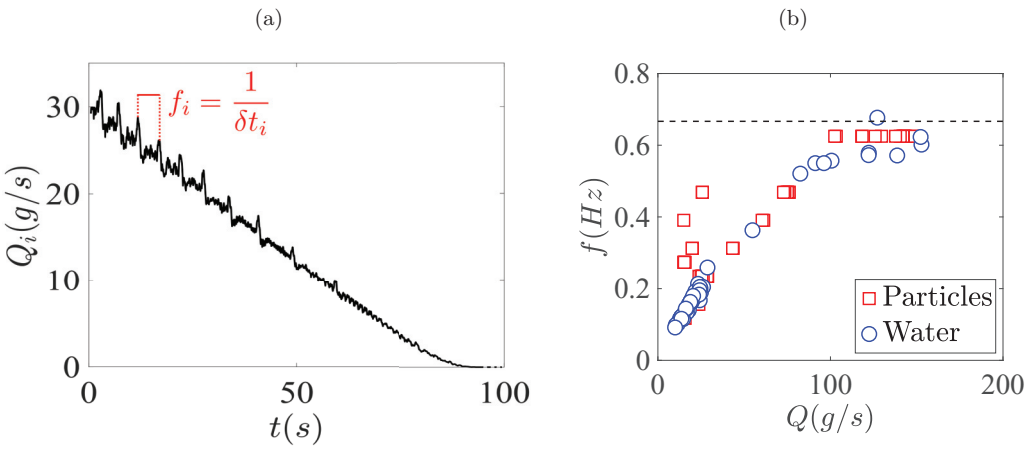

FIG. 14. (a) Temporal evolution of the discharge flow rate of the silo filled with water. (b) Frequency of the oscillation of the flow rate as a function of the discharge flow rate for the granular media and water. The dashed line represents the stabilization time of the electronic balance.

filled with water with the outlet slightly immersed in a large reservoir of water and a small outlet size $D \approx 5$ mm. In Fig. 14(a) we observe that the flow rate decreases with time, in agreement with the classical Torricelli law, but also that the signal exhibits fluctuations similar to the granular case. Figure 14(b) shows the frequency of oscillation as a function of the mass flow rate for both the discharge of the water and the granular media. For both cases, the data are superimposed and we observe that the frequency of oscillation increases as the discharge flow rate increases, and saturates for a large flow rate. This suggests that this effect is linked to the electronic balance response time rather than to actual flow rate fluctuations. Indeed, the constructor specifies that the electronic scale has a response time of about 1.5 s for catching a rapid variation of the mass signal, and the saturated frequency value corresponds approximately to this stabilization time [see the dashed line in Fig. 14(b)]. Therefore, the oscillations of the signal of the flow rate are not considered in this paper.

APPENDIX B: SILO DISCHARGE IN WATER WITH A CONSTANT AIR FLOW RATE AT THE TOP

To evaluate the air pressure at the outlet for a discharge flow in water, we performed a steady experiment where we inject a constant volumetric flow rate of air at the top of the silo. We use a silo of diameter $L = 40$ mm with an outlet size $D = 10$ mm and ceramic particles of diameter $d_p = 180$ μm. We impose a constant volumetric flow rate of air, $Q_{\text{air}} \approx 6$ L/min, and we vary the water depth h_w between 0 and 16 cm, as can be seen in Figs. 15(a) and 15(b).

Figure 15(c) represents the temporal evolution of the particle flow rate for $h_w = 44$ mm. We observe that the instantaneous flow rate first decreases at the beginning of the discharge, due to the initial condition in which we manually remove the rubber plug after turning on the air flow. Then it reaches a steady flow similar to a discharge in air [20]. The mean flow rate Q is determined during this steady discharge period (red solid line), and the red dashed line represents the flow rate driven by gravity Q_0 in air. Therefore, we observe an increase of the flow rate that we relate to the additional driving force induced by the air flow rate. In Fig. 15(d), we plot the mean flow rate versus h_w, and we observe no dependency on this parameter. Indeed, a constant volumic flow rate of air at the top of the silo imposes a constant pressure gradient at the outlet. The analytical model for a steady discharge flow [Eq. (8)] gives a fairly good prediction of the discharge flow rate, independently of the surrounding fluid (see the dashed line).

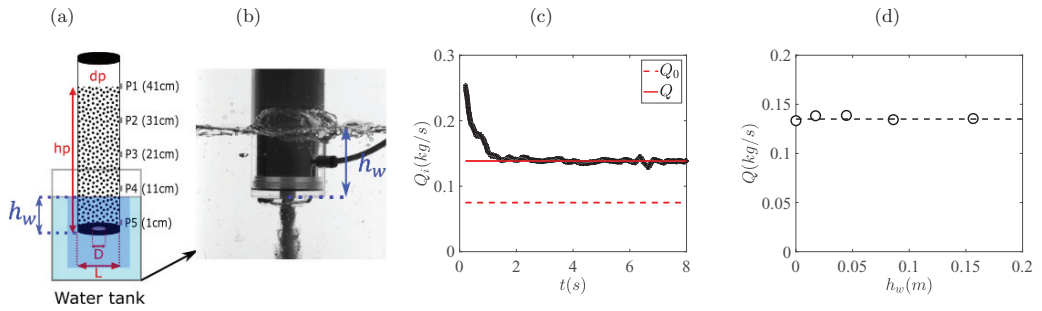

FIG. 15. Silo discharge in water: (a) Experimental setup displaying the position of the pressure sensors. (b) Typical picture during the discharge showing the definition of h_w. (c),(d) Discharge flow of ceramic particles in water with $d_p = 180$ μm for $L = 40$, $D = 10$ mm, and $Q_{\text{air}} \approx 6$ L/min. (c) Temporal evolution of the instantaneous discharge flow rate for ceramic particles with $d_p = 180$ μm, $L = 40$ mm, $D = 10$ mm, $Q_{\text{air}} \approx 6$ L/min, and $h_w = 44$ mm. The full line represents the mean flow rate and the dashed line represents the gravity-driven flow rate Q_0. (d) Mean discharge flow rate as a function of the water depth h_w. The dashed line represents the analytical model for a steady discharge flow with a constant air flow rate at the top of the silo [Eq. (8)].

Figure 16 illustrates how the gas pressures within the silo [P_1 to P_5; see Fig. 15(a) for the positions of the sensors] vary during the silo discharge, for (a) the outlet in open air ($h_w = 0$ mm) and (b) $h_w = 85$ mm. We observe the same behavior for a discharge either in air or water: while the pressure tap is inside the granular column, the pressure is constant. However, we observe a shift of the pressure level between these two cases. To characterize this shift, we focus on the gas pressure level P_5, which is located near the silo outlet ($z_5 = 1$ cm).

Figure 16(c) illustrates the mean pressure level of P_5 during the discharge as a function of the water depth h_w. We observe a linear increase of the gas pressure near the outlet, corresponding to a slope equal to $\rho_w g$ (where ρ_w is the density of water), but with a small offset with the value corresponding to the outlet in open air ($h_w = 0$). This suggests that the surrounding liquid adds a hydrostatic overpressure at the outlet:

$$P^f_{\text{outlet}} = P_{\text{atm}} + \rho_w g(h_w + h_0), \tag{B1}$$

where P_{atm} represents the room air pressure, and $h_0 \approx 1$ cm accounts for the offset and allows best fitting of the data. Let us note that this length corresponds approximately to the height of a bubble

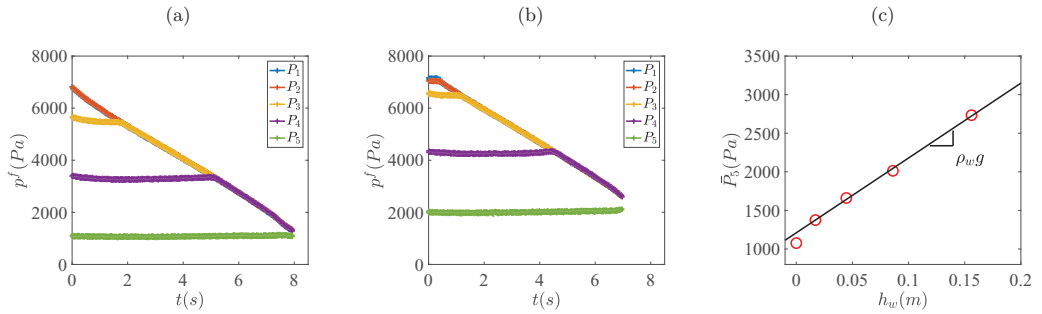

FIG. 16. Discharge of a silo with a constant volumetric air flow $Q_{\text{air}} \approx 6$ L/min for $L = 40$, $D = 10$ mm, and $d_p = 180$ μm (ceramic particles): (a),(b) temporal evolution of the pressure profiles within the silo P_1 to P_5 for (a) $h_w = 0$ mm (with the outlet in air) and (b) $h_w = 85$ mm; (c) mean value of P_5 during the discharge as a function of the water depth h_w. The full line represents Eq. (B1).

observed in the experiments and located beneath the bottom of the silo during the discharge, as can be seen in Fig. 15(b). While this hydrostatic overpressure has no influence on the particle flow rate for a constant Q_{air}, it plays a role in the case of a pressure-imposed discharge.

[1] G. H. L. Hagen, Über den Druck und die Bewegung des trocknen Sandes, Bericht über die zur Bekanntmachung geeigneten Verhandlungen der Königlich Preussischen Akademie der Wissenschaften zu Berlin, 35–42 (1852).

[2] B. P. Tighe and M. Sperl, Pressure and motion of dry sand: translation of Hagen's paper from 1852, Granul. Matter **9**, 141 (2007).

[3] S. M. Rubio-Largo, A. Janda, D. Maza, I. Zuriguel, and R. C. Hidalgo, Disentangling the Free-Fall Arch Paradox in Silo Discharge, Phys. Rev. Lett. **114**, 238002 (2015).

[4] P.-Y. Lagrée, L. Staron, and S. Popinet, The granular column collapse as a continuum: validity of a two-dimensional navier-stokes model with a μ(I)-rheology, J. Fluid Mech. **686**, 378 (2011).

[5] L. Staron, P.-Y. Lagrée, and S. Popinet, Continuum simulation of the discharge of the granular silo, Eur. Phys. J. E **37**, 5 (2014).

[6] S. Dunatunga and K. Kamrin, Continuum modelling and simulation of granular flows through their many phases, J. Fluid Mech. **779**, 483 (2015).

[7] G. Daviet and F. Bertails-Descoubes, Nonsmooth simulation of dense granular flows with pressure-dependent yield stress, J. Non-Newtonian Fluid Mech. **234**, 15 (2016).

[8] Y. Zhou, P. Y. Lagrée, S. Popinet, P. Ruyer, and P. Aussillous, Experiments on, and discrete and continuum simulations of, the discharge of granular media from silos with a lateral orifice, J. Fluid Mech. **829**, 459 (2017).

[9] G. D. R. MIDI, On dense granular flows, Eur. Phys. J. E **14**, 341 (2004).

[10] P. Jop, Y. Forterre, and O. Pouliquen, A constitutive law for dense granular flows, Nature (London) **441**, 727 (2006).

[11] Y. Forterre and O. Pouliquen, Flows of dense granular media, Annu. Rev. Fluid Mech. **40**, 1 (2008).

[12] W. A. Beverloo, H. A. Leniger, and J. Van de Velde, The flow of granular solids through orifices, Chem. Eng. Sci. **15**, 260 (1961).

[13] A. Janda, I. Zuriguel, and D. Maza, Flow Rate of Particles through Apertures Obtained from Self-Similar Density and Velocity Profiles, Phys. Rev. Lett. **108**, 248001 (2012).

[14] R. M. Nedderman, U. Tūzūn, and R. B. Thorpe, The effect of interstitial air pressure gradients on the discharge from bins, Powder Technol. **35**, 69 (1983).

[15] J. A. H. de Jong, Vertical air-controlled particle flow from a bunker through circular orifices, Powder Technol. **3**, 279 (1969).

[16] J. A. H. de Jong and Q. E. J. J. M. Hoelen, Cocurrent gas and particle flow during pneumatic discharge from a bunker through an orifice, Powder Technol. **12**, 201 (1975).

[17] B. J. Crewdson, A. L. Ormond, and R. M. Nedderman, Air-impeded discharge of fine particles from a hopper, Powder Technol. **16**, 197 (1977).

[18] R. A. Altenkirch and R. Eichhorn, Effect of fluid drag on low Reynolds number discharge of solids from a circular orifice, AIChE J. **27**, 593 (1981).

[19] S.-S. Hsiau, C.-C. Hsu, and J. Smid, The discharge of fine silica sands in a silo, Phys. Fluids **22**, 043306 (2010).

[20] Y. Zhou, P.-Y. Lagrée, S. Popinet, P. Ruyer, and P. Aussillous, Gas-assisted discharge flow of granular media from silos, Phys. Rev. Fluids **4**, 124305 (2019).

[21] J. L. Lage, The fundamental theory of flow through permeable media from Darcy to turbulence, in *Transport Phenomena in Porous Media*, edited by D. B. Ingham and I. Pop (Pergamon, Oxford, 1998), pp. 1–30.

[22] M. Benyamine, M. Djermane, B. Dalloz-Dubrujeaud, and P. Aussillous, Discharge flow of a bidisperse granular media from a silo, Phys. Rev. E **90**, 032201 (2014).
[23] Y. Zhou, P. Ruyer, and P. Aussillous, Discharge flow of a bidisperse granular media from a silo: Discrete particle simulations, Phys. Rev. E **92**, 062204 (2015).
[24] Z. Zou, P. Ruyer, P.-Y. Lagrée, and P. Aussillous, Discharge of a silo through a lateral orifice: Role of the bottom inclination versus friction, Phys. Rev. E **102**, 052902 (2020).
[25] Z. Gu and H. Wang, Gravity waves over porous bottoms, Coastal Eng. **15**, 497 (1991).
[26] K. R. Hall, G. M. Smith, and D. J. Turcke, Comparison of oscillatory and stationary flow through porous media, Coastal Eng. **24**, 217 (1995).
[27] K. R. Rajagopal, On a hierarchy of approximate models for flows of incompressible fluids through porous solids, Math. Models Methods Appl. Sci. **17**, 215 (2007).
[28] T. Zhu, C. Waluga, B. Wohlmuth, and M. Manhart, A study of the time constant in unsteady porous media flow using direct numerical simulation, Transp. Porous Media **104**, 161 (2014).
[29] R. J. Lowe, U. Shavit, J. L. Falter, Je. R. Koseff, and S. G. Monismith, Modeling flow in coral communities with and without waves: A synthesis of porous media and canopy flow approaches, Limnol. Oceanogr. **53**, 2668 (2008).
[30] L. Staron, P.-Y. Lagrée, and S. Popinet, The granular silo as a continuum plastic flow: The hour-glass vs the clepsydra, Phys. Fluids **24**, 103301 (2012).
[31] http://basilisk.fr.
[32] http://basilisk.fr/src/poisson.h.
[33] R. O. Uñac, A. M. Vidales, O. A. Benegas, and I. Ippolito, Experimental study of discharge rate fluctuations in a silo with different hopper geometries, Powder Technol. **225**, 214 (2012).